BNL-220570-2020-JAAM

Unraveling Na and F coupling effects in stabilizing Li, Mn-rich layered oxide cathodes via local ordering modification

P. Vanaphuti, J. Bai

To be published in "ENERGY STORAGE MATERIALS"

October 2020

Photon Sciences

Brookhaven National Laboratory

U.S. Department of Energy

USDOE Office of Science (SC), Basic Energy Sciences (BES) (SC-22)

Notice: This manuscript has been authored by employees of Brookhaven Science Associates, LLC under Contract No. DE-SC0012704 with the U.S. Department of Energy. The publisher by accepting the manuscript for publication acknowledges that the United States Government retains a non-exclusive, paid-up, irrevocable, world-wide license to publish or reproduce the published form of this manuscript, or allow others to do so, for United States Government purposes.

DISCLAIMER

This report was prepared as an account of work sponsored by an agency of the United States Government. Neither the United States Government nor any agency thereof, nor any of their employees, nor any of their contractors, subcontractors, or their employees, makes any warranty, express or implied, or assumes any legal liability or responsibility for the accuracy, completeness, or any third party's use or the results of such use of any information, apparatus, product, or process disclosed, or represents that its use would not infringe privately owned rights. Reference herein to any specific commercial product, process, or service by trade name, trademark, manufacturer, or otherwise, does not necessarily constitute or imply its endorsement, recommendation, or favoring by the United States Government or any agency thereof or its contractors or subcontractors. The views and opinions of authors expressed herein do not necessarily state or reflect those of the United States Government or any agency thereof.

Unraveling Na and F coupling effects in stabilizing Li, Mn-rich layered oxide cathodes via local ordering modification

Panawan Vanaphuti[a], Jianming Bai[b], Lu Ma[b], Steven Ehrlich[b], Kim Kisslinger[c], Feng Wang[d], Yan Wang[a,*]

[a] Department of Mechanical Engineering, Worcester Polytechnic Institute, Worcester, MA 01609, USA
[b] National Synchrotron Light Source II, Brookhaven National Laboratory, Upton, NY 11973, USA
[c] Center for Functional Nanomaterials, Brookhaven National Laboratory, Upton, NY 11973, USA
[d] Sustainable Energy Technologies Department, Brookhaven National Laboratory, Upton, NY 11973, USA

ARTICLE INFO

Keywords:
Co-dope
Oxygen migration
Voltage fading
In situ XRD
In situ XAS

ABSTRACT

Regardless of the prevailing capacity and energy density of lithium, manganese-rich layered oxide (LMR-NMC) cathodes, continuous decay of voltage and overall energy density during cycling hinders this material from commercialization in Li-ion batteries. Although significant work focuses on single doping of Na and F, analysis in portraying the benefit of these ions in diminishing the structural distortion during activation cycle is in doubt. Herein, the effects of co-doping Na and F into the LMR-NMC structure in stabilizing the structure and mitigating oxygen loss during the first cycle are closely examined via in situ x-ray measurements. Na and F co-doping shows a 30% lower degree of Li^+/Ni^{2+} mixing in the Li layer (C2/m structure), 50% reduced Debye-Waller factor of Mn-O bonding, increase reversible TM migration, and faster Li diffusion relative to the pristine material. Due to the utilization of Ni redox chemistry below 4.4 V, less oxygen redox is required for charge compensation at high voltage. This study offers the first instance to quantitatively evaluate the effects of co-doping Na and F in LMR-NMC cathode in order to minimize voltage degradation by altering the local ordering of O3-type structure, which may rationalize strategies to overcome the issues of the material.

1. Introduction

The lithium, manganese-rich layered oxide cathode (LMR-NMC), $xLi_2MnO_3 \bullet (1-x)LiTMO_2$ (TM = Co, Ni, Mn), is remarkably attractive due to its high specific capacity of over 250 mAh g^{-1} between in the voltage range 2.0 – 4.8 V (vs. Li/Li^+). LMR-NMC can be ascribed as two phases, $LiTMO_2$ (R-3m space group) and Li_2MnO_3 (C2/m space group). Unlike other conventional cathodes, NMCs, $LiCoO_2$ and $LiFePO_4$, LMR-NMC delivers greater capacity, attributing to both cationic (transition metals) and anionic (oxygen) redox reactions [1,2].

Despite the high energy density of LMR-NMC, many challenges remain until it can be fully applied commercially: irreversible capacity loss after activation cycle, poor rate capability and voltage fading [3,4]. Many factors contribute to these problems such as activation of Li_2MnO_3-like phase, irreversible oxygen redox, TM migration to Li vacancies, layered-spinel transformation, surface reaction with electrolyte at high voltage and particle cracking [5]. Among various aspects, TM and oxygen migration during Li_2MnO_3-like phase activation, offering additional capacity through anionic redox asymmetry, are the main influences on voltage hysteresis and voltage decay of this material due to the variation of the cathode's density of state and rise of Fermi level [6,7]. This phenomenon introduces defect formation contributing to ~1 V hysteresis and the origin of voltage decay [6]. Recent studies revealed a fundamental understanding on the structural related issues of pristine LMR-NMC during cycling. Yet, there is still no clear pathway to the solution. In fact, out of all the techniques, surface coating and lattice doping are by far the most reliable and feasible methods [8,9].

Co-doping cations and anions is becoming one of the appealing methods to resolve the voltage degradation issue. Chen et al reported that doping Cd and S lessens volume changes during charging to high voltage (above 3.0 V) and enhances rate capability (153.8 mAh g^{-1} for co-doped sample vs 10 mAh g^{-1} for pristine sample at 5C) [10]. By the same means, Liu et al and Ming et al doped Na-F and Nb-F, respectively, into the LMR structure to achieve better structural stability [11,12]. Mg and F co-doping is reported by Lim et al to increase the discharge capacity (259 mAh g^{-1} for co-doped sample vs 248 mAh g^{-1} for pristine sample at 0.1C) and also cycle performance (90% capacity retention after 150 cycles) [13]. Due to their elemental abundance, cost effectiveness and

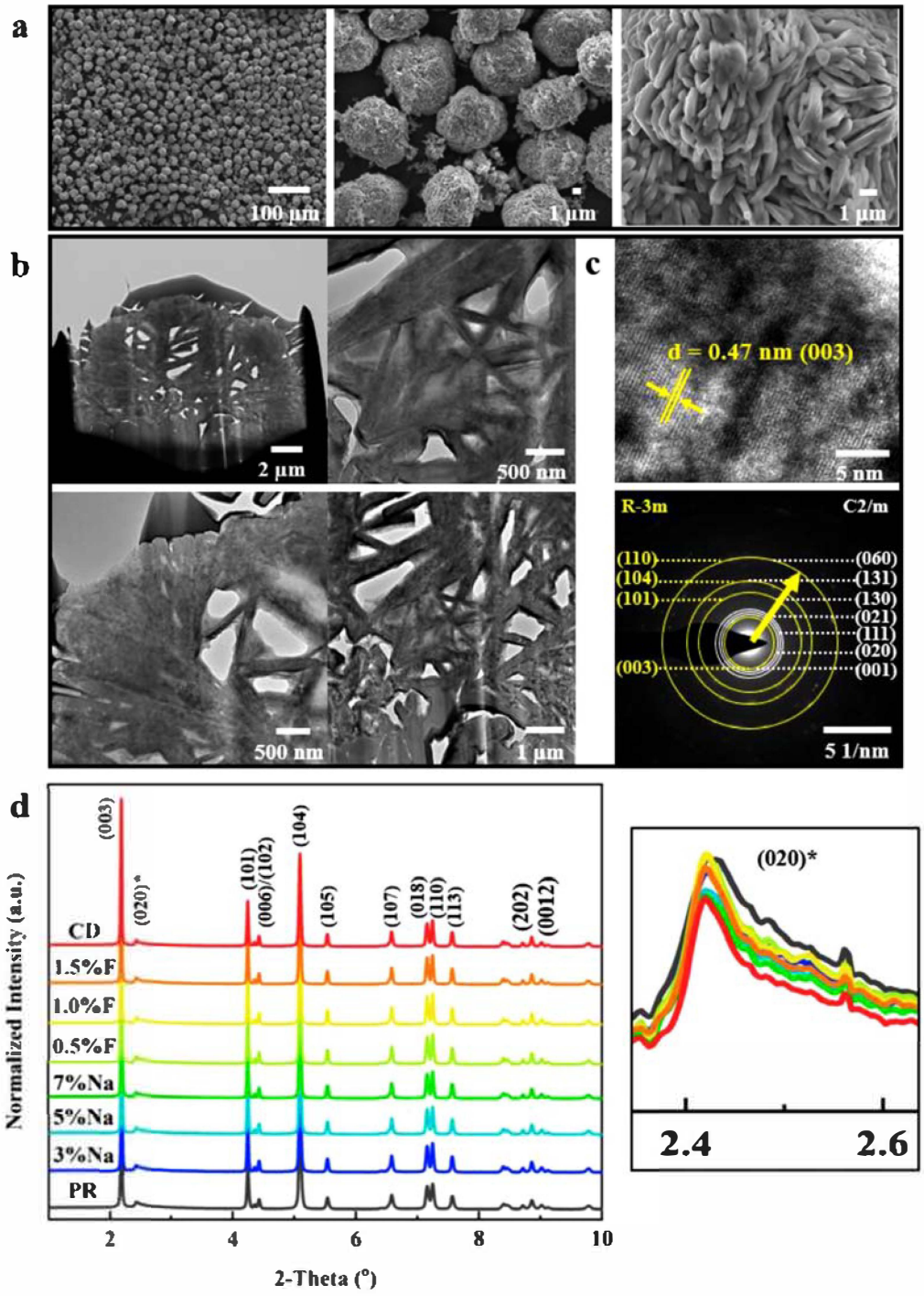

Fig. 1. Morphology and crystallinity of CD; (a) SEM images of the secondary particles, (b) Cross-sectional TEM images of an individual particle, and (c) HAADF STEM image taken at the center of the particle with its corresponding SAED pattern. (d) *Ex situ* synchrotron XRD (λ = 0.18208 Å) for eight samples with (020) plane of monoclinic structure (C2/m) on a magnified scale.

appropriate ionic size, Na and F are among the most common cation and anion to be examined, respectively. To facilitate the rate capability, Na is introduced into the structure to widen the Li layer, induce stacking faults and diminish cation mixing [14–18]. In the case of F, it is believed to play a significant role in suppressing voltage degradation, by substituting oxygen site, resulting in longer cycling life and reversible capacity of LMR-NMC [19–23]. Moreover, it is also claimed that LiF (act as F source) increases the cathode density, decreases surface area and minimizes electrolyte reactivity [24]. Ceder's group has also revealed the role of F theoretically and experimentally by density functional theory (DFT) calculations along with solid-state nuclear magnetic resonance (NMR) spectroscopy. By including F into the bulk of disordered rocksalt oxides, enhancement of electrochemical performance and average voltage, and decrease of oxygen loss are achieved due to the modification of short-range ordering of the local environment [24–26]. While significant effort shows that co-doping technique improves the electrochemical performance of LMR-NMC, the direct evidence and quantitative measurement on how lattice doping of both cation and an-

ion can provide additional benefits on retarding the voltage decay than single dopant remains unclear.

Based on our previous study, we co-doped LMR-NMC with Na and F elements via the conventional hydroxide co-precipitation route and solid-state reaction was successfully synthesized. Our co-doped sample (CD) shows both high capacity retention (97%) and high voltage retention (91%) over 100 cycles with initial discharge capacity of 260 mAh g^{-1} at 0.1C [27].

Unlike the electrochemical performance emphasis in the previous work, the main objective of this study is to elucidate the principle of Na and F incorporation into the LMR-NMC structure on unravelling the voltage fading and oxygen migration issue, especially during the activation cycle, via X-ray measurements. This paper is the first to report the quantitative analysis of structural stability affected by Na and F co-substitution. From *ex situ* XRD, CD cathode powder (before cycle) shows a 20% to 30% lower degree of Li^+/Ni^{2+} mixing in the Li layer as obtained from XRD refinement with the R-3m and C2/m models, respectively. After activation of first charge, the irreversibility of c-axis between first discharge and second charge of pristine (PR) and CD are 0.29% and 0.19%, respectively. This shows a clear indication of less structural distortion of the CD sample. While completion of first charge to 4.8V, the Debye-Waller factor (σ^2_{Mn-O}) of the CD sample is approximately 50% lower relative to PR, which provides the capability of CD to minimize the oxygen migration from the structure during the activation cycle. From the TM migration aspect, the σ^2_{Ni-TM} is reduced by approximately 76% akin to PR. Since the σ^2 term in the EXAFS equation accounts for the mean-square variation in path length, where variation corresponds to thermal or structural contributions, this work indirectly correlates the structural disorder of the fitted path due to oxygen and transition metal migration from the structure. This study offers a better understanding of co-doping Na and F in LMR-NMC cathode in order to minimize voltage degradation, which in turn, may enlighten a new strategy to overcome the issues for this material.

2. Results and discussion

2.1. Morphological and structural analysis

SEM images of CD secondary particles (Fig. 1a) show the uniform distribution of particle size. From the cross-section sample of CD, the high-angle annular dark field (HAADF) images (Fig. 1b) shows flake-like primary particles with noticeable porosity and agglomeration into spherical secondary particles. Each small flake is ~100-150 nm in thickness and the polycrystalline secondary particle size is ~14-17 μm. The high resolution TEM images taken from the center of the particle (Fig. 1c) show d-spacing of ~4.7 Å ((003) plane) with the corresponding selected area diffraction (SAED) pattern. All the planes are well-matched with layered R-3m and C2/m structure.

The elemental ratio from EDS for both PR and CD samples are verified (Fig. S1). All elements were detected by EDS showing uniform distribution across the particle, except F because of the overlapping of Mn L_α energy with F K_α energy. Detailed electrochemical performance is presented in our previous report [27]. Predominantly, CD has higher specific capacity (~25 mAh g^{-1} at every tested C-rate) and better voltage retention capability (91% vs. 84% after 100 cycles) than PR. In addition, the initial charge-discharge profile of PR and CD is compared in Fig. S2. CD sample shows a slightly greater capacity below 4.5 V (approximately ~10 mAh g^{-1}), reversible oxygen redox, and higher voltage during discharge compared to PR sample.

In order to examine the Li^+ diffusion kinetics during the first charge process, the galvanostatic intermittent titration technique (GITT) is analyzed (Fig. 2a). By comparing the voltage response from each small current pulse, qualitative information on Li^+ diffusion kinetics is achieved. Evidently, the voltage response (ΔEt and ΔEs) and polarization of CD is smaller than those of PR below 4.4 V, corresponding to Ni and Co oxidation region (expanded curve). The higher increment of voltage is

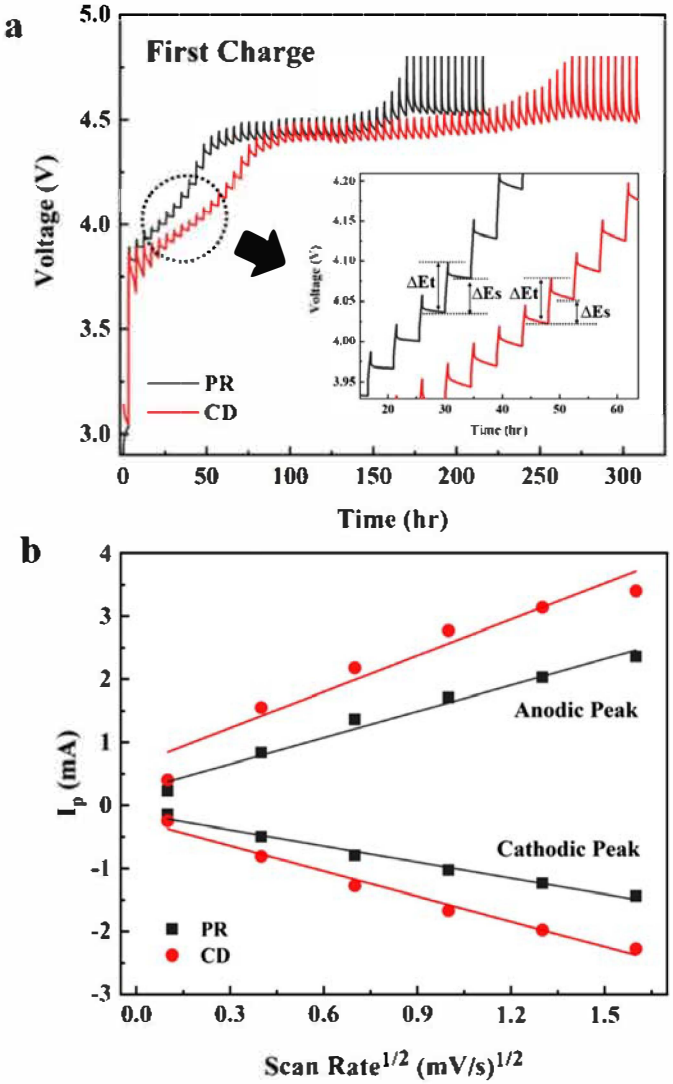

Fig. 2. Ionic conductivity test for PR (grey) and CD (red) samples; (a) galvanostatic intermittent titration technique (GITT) curves during first charge where each step consists of 30-minute current pulse at 0.05C and 4-hour relaxation period, and (b) plot between anodic/cathodic peak current (I_p) vs. scan rate ($v^{1/2}$) from the CV curves in Fig. S3.(For interpretation of the references to color in this figure legend, the reader is referred to the web version of this article.)

related to the internal resistance; therefore, this confirms that the Na and F dopants facilitate the Li^+ diffusion. Beyond 4.4 V (O oxidation region), the curves are similar for both samples. Due to the sluggish activation kinetics of LMR-NMC material, the steady-state voltage condition cannot be reached even with 4-hour relaxation period leading to the difficulty of attaining quantitative analysis of Li diffusion coefficient [28,29]. Alternatively, the cyclic voltammetry (CV) with various scan rate was then employed to calculate the Li diffusion coefficient (D_{Li+}) using Randles-Sevcik Eq. (1) where n is the no. of electrons transfer per reaction (in this case n = 1), A is the electrode surface area (1.13 cm^2) and C is the molar concentration of Li-ion in LMR-NMC [30].

$$I_p^2 = \left(2.69x10^5\right)^2 n^3 A^2 D_{Li+} v C^2 \quad (1)$$

The plot of anodic/cathodic peak current (I_p) vs. scan rate ($v^{1/2}$) (Fig. 2b) from the different scan rate of CV curves when applying voltage between 2.50 – 4.80 V is shown in Fig. S3. The slope is proportional to Li^+ kinetics in which the steeper the slope, the faster the Li^+ diffusion is. Note that the peak around 3.9 V (anodic peak) and around 3.7 V (cathodic peak) corresponds to the Ni/Co oxidation and reduc-

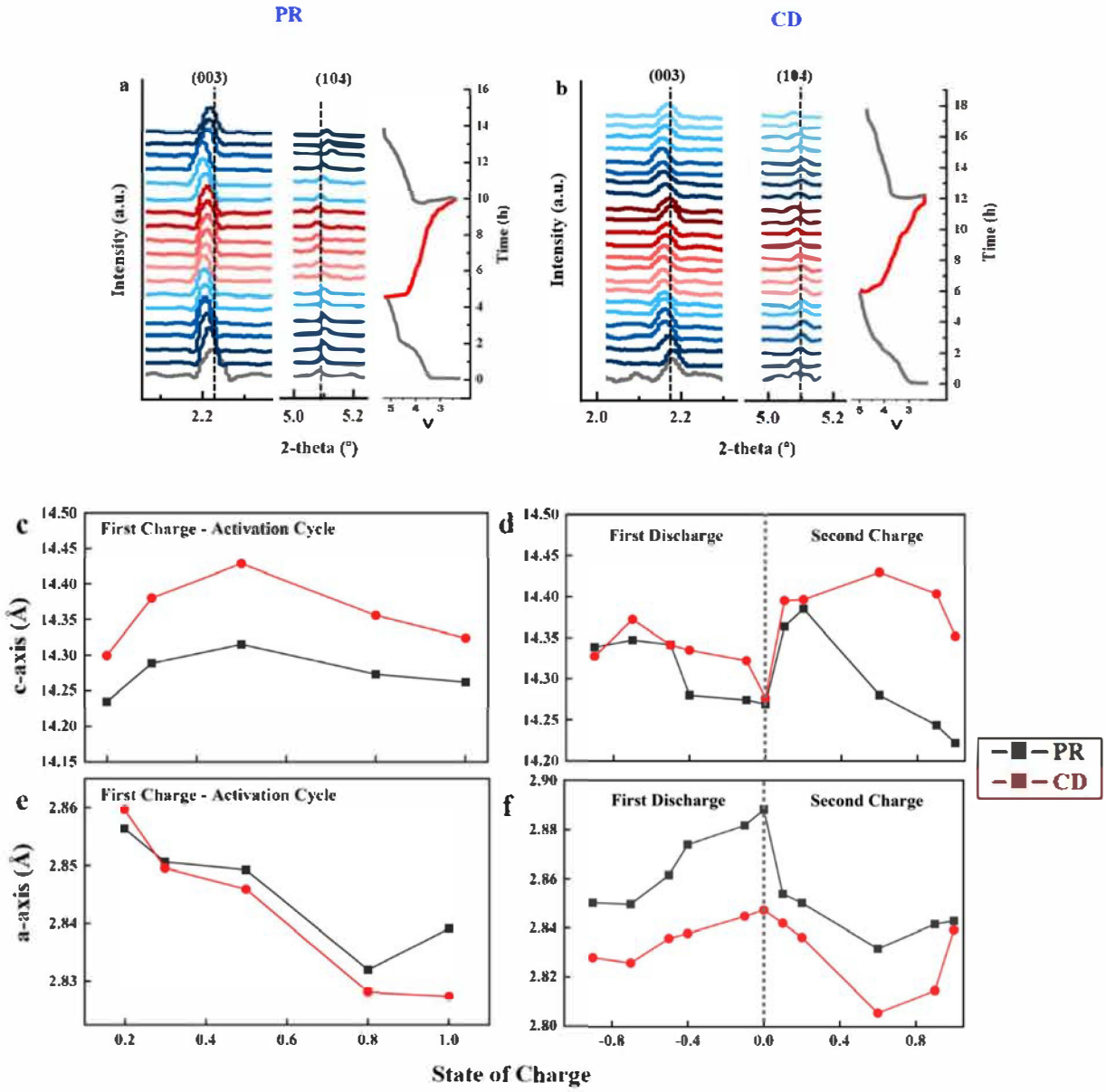

Fig. 3. *In situ* XRD patterns collected with synchrotron radiation (0.18208 Å) during charge and discharge from 2.50 – 4.80 V and voltage profile for (a) PR (grey) and (b) CD (red). Lattice parameters vs. state of charge/discharge for the corresponding cycles; (c) c-axis of first charge, (d) c-axis of first discharge and second charge, (e) a-axis of first charge, and (f) a-axis of first discharge and second charge. The XRD pattern collected at open circuit potential (OCP) state of the *in situ* battery are plotted in gray.

tion, respectively. These two peak currents are used to calculate D_{Li+} from Eq. (1) since Ni/Co are more redox active than Mn. As expected, the slope of both anodic and cathodic peak (Fig. 2b) at different scan rate is steeper for CD than PR sample. Besides, the current peak of PR also shifts to higher voltage during charging and lower voltage during discharging compare to CD, which indicates a greater degree of polarization. Based on the anodic peak, the D_{Li+} equal to $1.27x10^{-11}$ cm^2 s^{-1} and $3.33x10^{-11}$ cm^2 s^{-1} for PR and CD samples, respectively. Meanwhile, D_{Li+} for cathodic peak of PR and CD samples are $4.60x10^{-12}$ cm^2 s^{-1} and $1.21x10^{-11}$ cm^2 s^{-1}, respectively. Evidently, CD sample has 2.6 times better diffusion rate than PR sample, which is further analyzed with *in situ* XRD in the next section.

2.2. Lattice distortion and structure integrity: In situ XRD

To gain better understanding of the structural changes due to Na and F dopants and their impact on the structural stability during cycling, *ex situ* and *in situ* XRD measurements were conducted. Quantitative structural analysis via Rietveld refinement was calculated on *ex situ* XRD patterns (Fig. 1d) using two structure models, R-3m and C2/m. Main results were provided in Fig. S4, Fig. S5, Table S1, and Table S2. Due to the insensitivity of x-rays to the difference in transition metal elements, some of the site occupancy parameters are fixed in the refinements, with values either from the nominal composition formula or neutron diffraction analysis on a similar system [31]. Constraints are applied to Li occupancy parameters to ensure the overall Li amount close to the value given in the composition formula.

Apart from enlarging the lattice parameters and unit cell volume in doped samples, both model structures of R-3m and C2/m have good agreement in showing well-ordered layered structure for all the samples, while greater reduced cation mixing is observed in the CD sample due to Na and F co-doping [11,32]. Compared to PR, the degree of Li^+/Ni^{2+} mixing is lower, approximately 20% to 30% in CD, as ob-

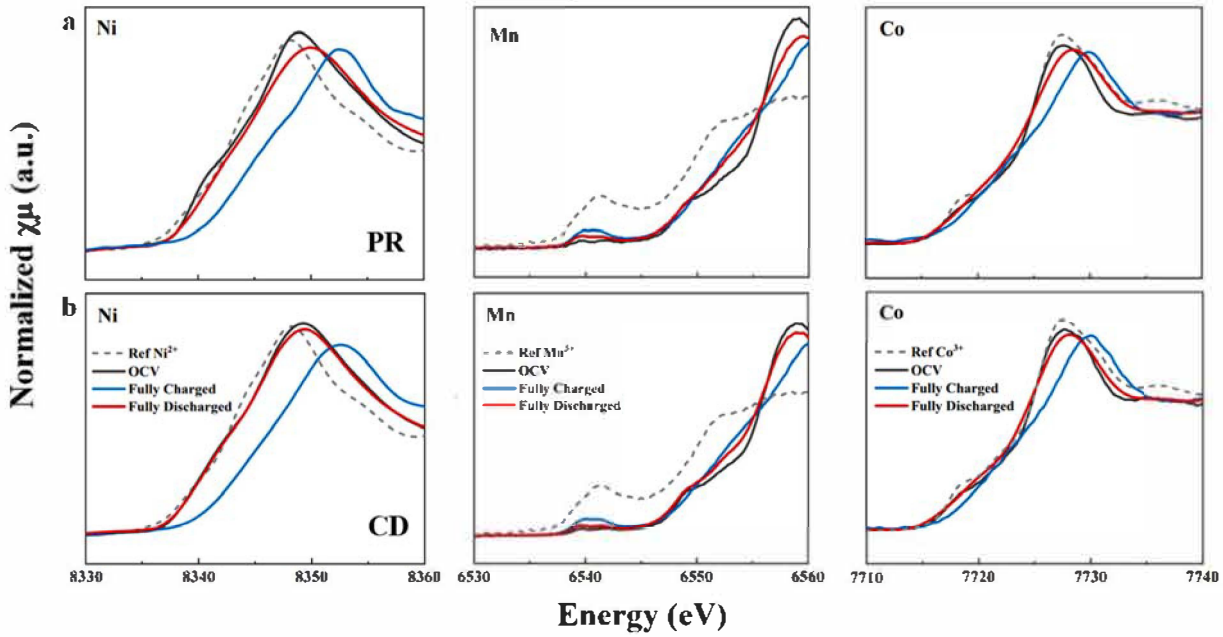

Fig. 4. X-ray absorption near edge structure (XANES) spectra of Ni, Mn, and Co valance state at OCV (grey), fully charged to 4.80 V (blue), and fully discharged (red) to 2.50 V for (a) PR and (b) CD samples.

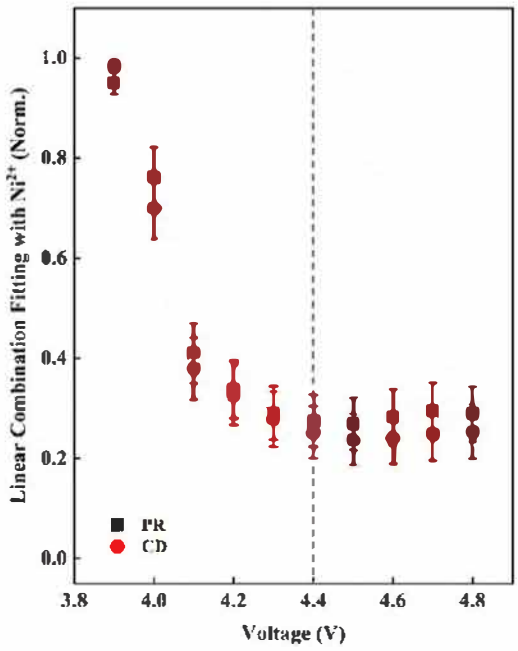

Fig. 5. Linear combination fitting of Ni oxidation state from XANES data in Fig. S6 between Ni(II)O and OCV state for different charged states of PR (grey) and CD samples (red).

tained from the XRD refinement with R-3m and C2/m model, respectively. From a close-up view of the superlattice peak of C2/m structure at ~2.45° (λ = 0.18208 Å) assigned to $LiMn_6$ cation ordering shows that the doped samples give slightly sharper feature than PR, which is consistent with the refinement data in Table S2 displaying less amount of Ni in Li position (4h site) and better cation ordering, especially for Na-doped samples. Notably, the apparent Ni occupancy is higher for Na doped samples, particularly for the 2b site in the C2/m structure. Since we did not specifically add Na ions in our refinement models, the increase in Ni occupancy is used as an indicator for Na doping, as when Li ions are replaced by Na, the effective electron number will increase on these sites. Although the doping amount of Na is relatively small, we observe that Na prefers to replace the Li site within the TM layers (3b in R-3m and 2b in C2/m) since the refinement result does not show an obvious change in Ni mixing in the Li layer (3a in R-3m and 4h in C2/m). However, the trend is not proportional with the amount of Na doping and this may be due to the variation of the Na amount in the measured sample with such small doping.

In situ XRD patterns were collected during charge and discharge between 2.50 – 4.80 V for 1.5 cycles. Representative XRD patterns and related results are presented in Fig. 3 and Table S3. At different states, lattice parameters are calculated using the (003) and (104) peaks based on R-3m. During initial charge, the c-axis increases due to Li extraction from the Li layer, and a-axis decreases as a consequence of oxidation of TM metals [33]. An opposite phenomenon occurs for the discharge state. Both samples have the same trend, however, CD shows higher lattice change, by ~0.3% (at 4.5 V) compared to PR due to higher amount of Li insertion/deinsertion via Ni^{4+}/Ni^{2+} redox below 4.4 V. There are three reasons to explain this: (1) Na/F widens the Li slab to facilitate the Li diffusivity (Tables S1 and S2), (2) Na reduces Li^{+}/Ni^{2+} mixing, especially for Li_2MnO_3-like structure, and (3) F utilizes the Ni^{2+} redox-active due to lower valence of F relative to O. In order F^{-} to accommodate O^{2-} sites, TM metals, including active redox Ni, are partially reduced to Ni^{2+} to retain the charge balance. As a result, additional specific capacity is achieved for CD than PR, 260 mAh g^{-1} vs 235 mAh g^{-1} at 0.1C [27]. C-axis of PR and CD layered structure expands 0.0269 and 0.0246, respectively, when charging up to 4.8 V (Fig. 3c). After activation during the first charge, the irreversibility of c-axis between first discharge and second charge of PR and CD are contracted 0.29% and expanded 0.19%, respectively (Fig. 3d and Table S3). CD shows a higher percent of structural integrity, which is related to the lower quantity of O 2p redox forming unstable peroxo-like O and TM migration during activation cycle from F substitution [25,26]. This is consistent with the columbic efficiency of first cycle for PR and CD, 74% and 81%, respectively. Although, the differences are relatively small, the consequence of this irreversible TM and O 2p redox on voltage degradation after first cycle is substantial, which will be further expounded in the next section [34–37].

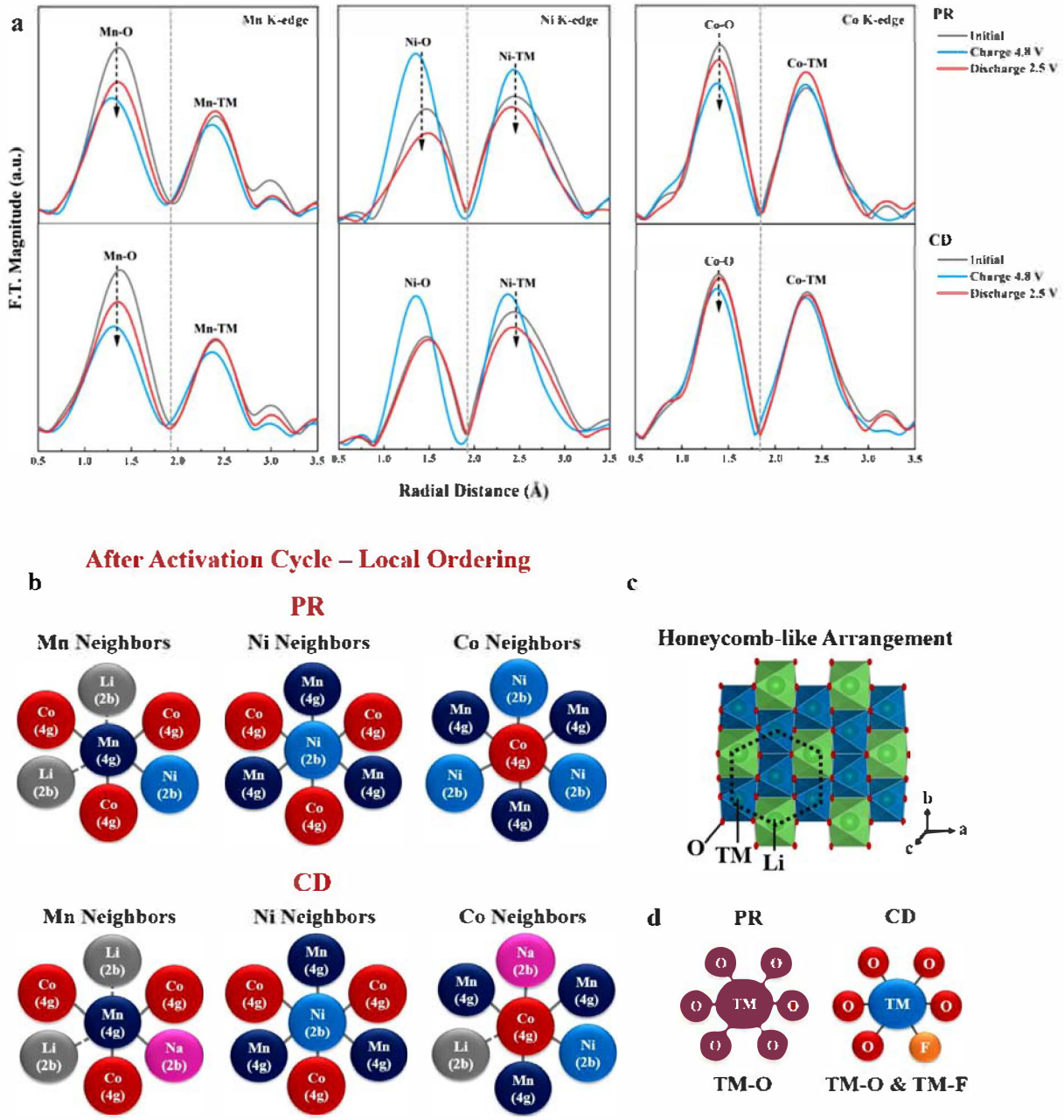

Fig. 6. (a) Extended X-ray absorption fine structure (EXAFS) spectra of Mn, Ni and Co during initial state (grey), first charge (blue), and first discharge (red) from 2.50 – 4.80 V for PR (top) and CD (bottom). The spectra show two important features; ~1.3 Å (reduced distance) and ~2.5 Å (reduced distance) identify TM-O and TM-TM interaction, respectively. (b) Predicted local cation ordering of Mn, Ni and Co after first discharge to 2.5 V for PR and CD samples. (c) Illustration of honeycomb-like arrangement in C2/m space group. (d) Predicted short-range ordering of TM with O and F in PR and CD, respectively.

2.3. Cationic redox, anionic redox and local ordering: In situ XAS

While both Na and F effects are elucidated via XRD, the role of F is explained with in situ XAS as it is correlated to the oxygen environment. TM redox, local ordering and oxygen redox during first cycle are closely observed via *in situ* XAS measurement during first charge (0.1C) and discharge (0.2C) between 2.50 and 4.80 V. XANES plots for each TM metal (Mn, Ni, Co) are illustrated in Fig. S6 whereas the change after completed the first cycle is compared in Fig. 4. Clearly, the initial OCV state and after fully discharged to 2.5 V for CD sample is almost completely reversible which indicates the prevention of Ni^{3+} or Mn^{2+}/Mn^{3+} formation. As predicted, transition metals, mostly from Ni, undergo oxidation (shift to higher energy) during charging below 4.4 V (providing ~120 mAh g^{-1}) and vice versa of the redox process during discharge. Both samples show small change in Mn *K*-edge absorption during first charge resulting from the structural distortion of MnO_6 octahedra (Jahn-Teller effect of Mn^{3+}) and the insignificant reduction of Mn^{4+} to Mn^{3+} in the low voltage region (~20 mAh g^{-1}) [38–40]. Ni plays a significant role in providing the capacity for LMR-NMC material under 4.4 V, specifically Ni^{2+} to Ni^{4+} between 3.8 - 4.2 V, as seen in the obvious shifting of energy for both samples [41,42]. Interestingly, linear combination fitting in Fig. 5 shows a noticeable increase of Ni^{2+} to Ni^{4+} (around 4.2 V) of CD in contrast to PR and, correspondingly, the larger alteration in lattice parameters was observed by *in situ* XRD and smaller voltage response (less resistance for Li^+ kinetics) by GITT measurements as described in the previous sections. Beyond 4.4 V, the Ni^{2+} quantity becomes more

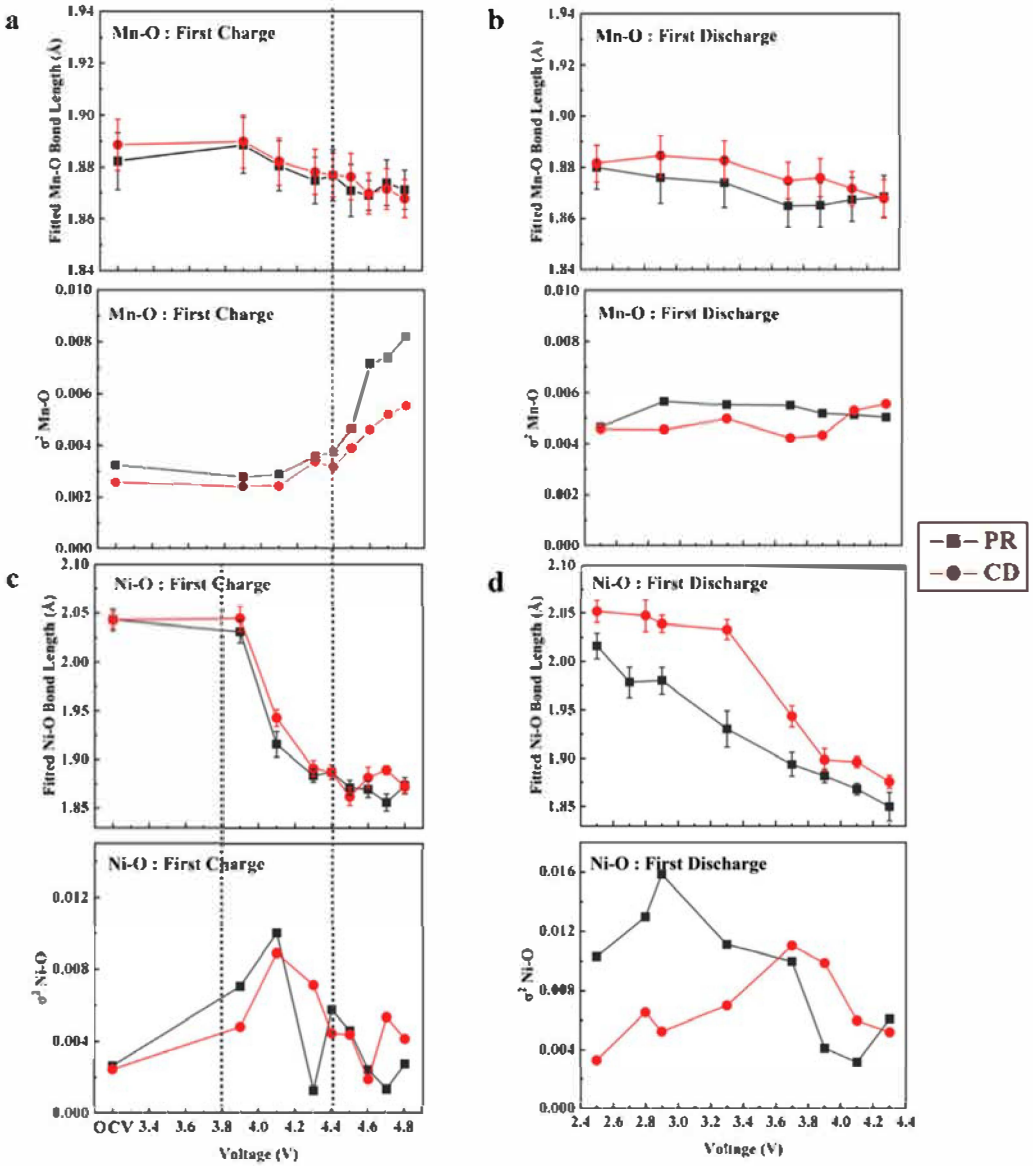

Fig. 7. Fitted TM-O bond length and Debye-Waller factor (σ^2_{TM-O}) from EXAFS spectra of first shell coordination for PR (grey) and CD (red) samples; (a) Mn-O bond length and σ^2_{Mn-O} during first charge, (b) its corresponding first discharge, (c) Ni-O bond length and σ^2_{Ni-O} during first charge, and (d) its corresponding first discharge. Fitted profile of TM K-edge EXAFS spectra in k-space and R-space are shown in Fig. S12 for OCV state of PR and CD samples.

stable but increases slightly, possibly due to charge compensation after partial loss of TM and O, which shows the same trend for PR and CD. With regarding to O 2p orbital redox at high voltage, there are two ways for oxygen to provide excess capacity: redox reaction of $O^{2-}/(O_2)^{n-}$ (n < 2) ions (forming electron holes) and O_2 gas release from the structure [43,44]. The latter, usually from O redox near the surface, reacts with the electrolyte to form CO_2.

Fig. 6a shows the EXAFS spectra of each TM metal for the first activation cycle. All TM-O bonds decrease upon first charge. Both Mn-O, Ni-O and Ni-TM coordination is significantly depopulated after first discharge, attributing to the partially irreversible TM migration and generation of oxygen vacancies. In fact, oxygen vacancies are the major driving force for Mn migration due to the decrease in energy barrier, especially for the Li_2MnO_3-like structure. For Co, it is negligible as reported in a previous study [37]. These transition metals move from octahedral sites of TM layer to new tetrahedral sites of Li layer, triggered by a high Li vacancy concentration at high voltage, and form an inactive spinel phase (lead to bulk densification) at prolonged cycles. This is thermodynamically favorable since the energy of new sites in the Li layer in O3-type structure is lower due to the weaker edge-sharing cations repulsion than the O2-type structure, where the repulsion of face-sharing cations is much stronger, and in turn, hinders the TM migration [7]. In contrast, CD restores local ordering of Mn-TM, Ni-O and Co-TM, and less changing in the Ni-TM and Mn-O bond after completed first discharge; this demonstrates a better conservation of O3-type structure [40,42]. As all TM-O and TM-TM environment of CD is apparently minimized, it is appropriate to say that F substitution in CD reduces TM migration and O 2p redox by the strong tendency of Li-Mn ordering and TM-F interaction.

Predicted cation ordering after activation cycle from EXAFS spectra is presented in Fig. 6b using a honeycomb-like arrangement (Fig. 6c) as the ordering of this superstructure plays significant roles in causing voltage decay from the change in coordination around O^{2-} due to TM migration at high voltage, thereby, lowering the discharge potential of O redox [43,45,46]. Mn and Co have a similar environment, occupying the 4g site, where Mn is surrounded with the highest amount of Li (from the least intensity of Mn-TM bonding) and partially bonded with Co. Analo-

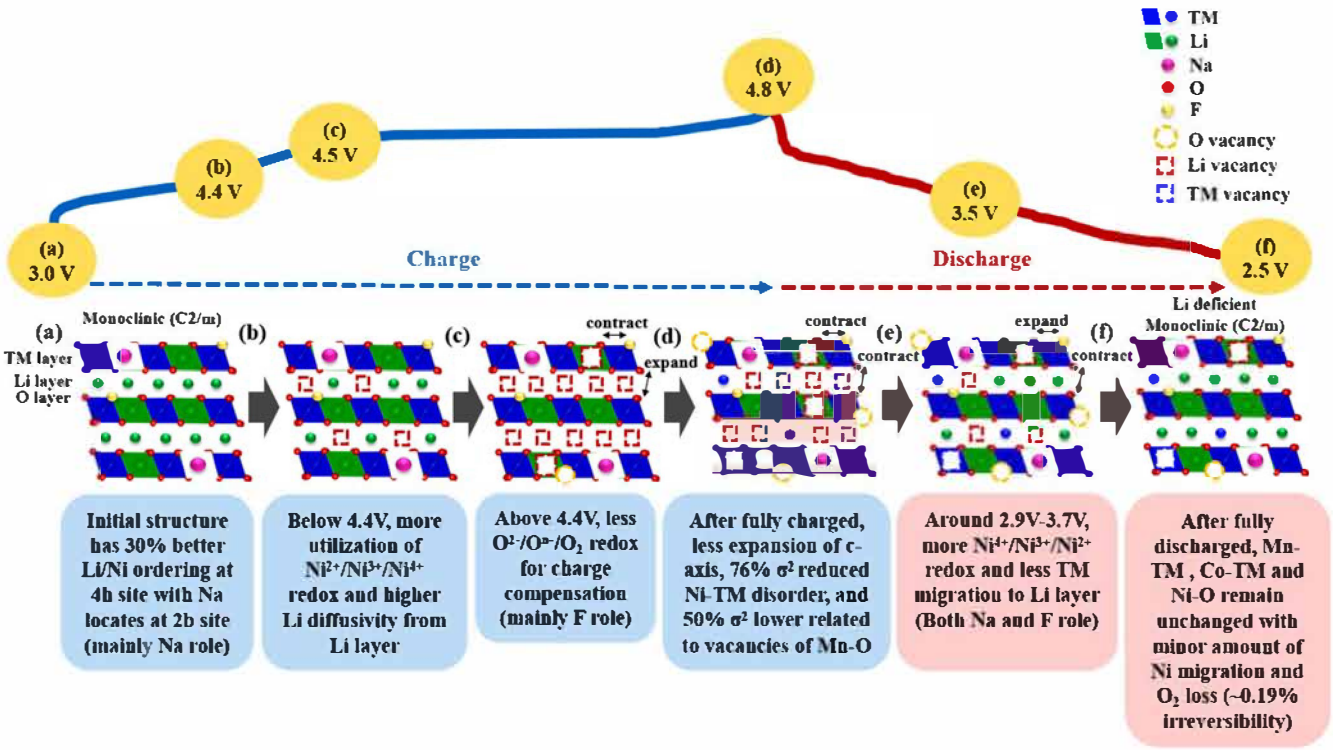

Fig. 8. Mechanism of Na and F (CD) in LMR-NMC lattice to offer struture stabilization during different charge/discharge states of initial cyclebased on C2/m structure model.

gous to Mn, Co bonds to Mn/Ni/Li, however, less bonding with Li exists because the intensity of Co-TM is greater than Mn-TM. In contrast, Ni (2b site) is bonded only to TM (Mn and Co in 4g site). This is correlated with the higher intensity of Ni-TM than Ni-O bonds. Na substitution is likely to be in the 2b position referring to XRD refinement data. Comparing CD to PR after completed first cycle, more Li and less Ni presents in 2b site due to less cation mixing at high voltage and TM migration from strong TM-F interaction in short-range ordering (Fig. 6d). Additionally, Fig. S7 presents a closed-up view of Mn-O bonding at various charge states. As expected, slightly higher retention of Mn-O bonding is observed for CD than PR because the differences between initial state and 4.8 V is narrower.

To better exploit the effect of F substitution in utilizing redox-active Ni reservoir, lowering TM migration and mitigating O redox asymmetry, EXAFS fitting of Mn and Ni local ordering at various states of charge has been interpreted. Note that fitting in Artemis software only allows atomic sites with full occupancy, thus, the structure models used in the calculation are based on Li_2MnO_3 and $LiNiO_2$ for C2/m and R-3m structure, respectively. The corresponding plot of Mn-O bond length and σ^2_{Mn-O} is shown in Fig. 7a and 7b during the activation cycle, and Fig. S8 for second charge. Table S4 provides the raw data. While Mn-O bond length does not have substantial alteration due to inactive Mn^{4+}, σ^2_{Mn-O} is significantly increased between 4.4 – 4.8 V for PR (50% higher compared to CD). Evidently, this identifies the increase in vacancies and angle distortion of Mn-O ordering, which initiates around 4.1 V and protrudes beyond 4.4 V.

Below 4.1 V, Li ions are mainly removed from the Li layer, in contrast to above 4.1 V, extraction of Li in both Li layer and TM layer occurs (high concentration of Li vacancy) resulting in Li_2MnO_3-like disorder, markedly in PR than CD. The relationship between σ^2 and bond vacancies has also been described in the Ru-O system. [47] There is also a small change in σ^2_{Mn-O} during second charge for PR, whereas both PR and CD do not have obvious change during discharge. Thus, there is no oxygen loss occurs and the structure is considered reversible after first charge. Supposedly upon cycling, most C2/m structural ordering is more reversible for CD than PR from the comparison of σ^2_{Mn-O} value. Additionally, Ni-O and Ni-Ni interactions during 1.5 cycles are analyzed to compare with Mn-O as shown in Fig. 7c and 7d, Fig. S9 and S10. Raw data are illustrated in Table S5. During the first charge, Ni-O bond length decreases due to the change from Ni^{2+} to Ni^{4+} primarily from Li removal of Li layer in both $LiTMO_2$ and Li_2MnO_3-like structures, which is the most pronounced at 3.8 – 4.3 V, and Ni-O bond length increases (Ni^{4+} to Ni^{3+}) at 2.9 – 3.7 V during discharge. This is the reason for larger distortion of σ^2_{Ni-O} value around 3.8 V – 4.3 V and below 3.7 V during discharge. The finding is well-consistent with NMR spectroscopy where the delithiation/lithiation happens at different paths; Li from $LiTMO_2$ structure is first removed during charge and Li_2MnO_3-like structure is first inserted during dischage [37]. Less change of σ^2_{Ni-O} value for CD indicates less loss of structural order and vacancy formation in the material after activation cycle. In fact, PR shows more decrease in bond length than CD during this potential range, especially at the first cycle, which can be related to a different pathway of Ni oxidation; Ni^{2+} to Ni^{4+} in PR and Ni^{2+} to Ni^{3+} to Ni^{4+} in CD. The formation of Ni^{3+} intermediate is supported by the recent work from Ceder's group on F substitution in disordered rocksalt cathode [25]. This phenomenon provides a better use of Ni redox and also lessens the amount of O for anionic redox asymmetry (decrease O_2 formation). We note that only 1% mol F is doped into LMR-NMC structure in this study and more differences may exist for a higher quantity of F substitution. Meanwhile, a high amount of F can degrade specific capacity due to the stable Li-F bond formation. In view of TM migration to adjacent Li layer, variation in σ^2_{Ni-TM} is used to indirectly explain this process since the EXAFS spectra of Ni environment shows the most changes after the first cycle and the proposed local ordering (Fig. 6b) shows a Ni-Mn correlation. Note that O vacancies favor the Mn migration in O3-type structure upon charge above 4.4 V. CD shows 76% lower differences of σ^2_{Ni-TM} after finishing the first cycle, contributing to smaller TM migration.

This local disordering and vacancy generation, dominated in PR, can be clearly detected above 4.4 V of initial charge and below 3.8V of discharge where σ^2_{Ni-TM} is the most fluctuated resulting from Mn/Ni

migration to Li layer as described previously. After the first cycle, the differences of σ^2_{Ni-TM} is decreased (Fig. S10c), which is attributed to the hysteresis reversibility. Note that the k-space signal becomes noisy above 8 Å, therefore, the fitted Ni-TM correlation is only used for relative observation.

According to molecular Fermi level aspect, owing to stronger electronegativity of F (3.98) compared to O (3.44), this reduces the energy difference between t_{2g} and e_g orbitals resulting in the weakening covalent interaction of TM-to-ligand charge transfer, thereby suppressing TM migration to a certain degree and rising average voltage from conventional inductive effects. In other words, electrons are more localized with F dopant. Moreover, Fig. S11 provides another indication for cycling stability improvement of CD after 200 cycles. The local cation ordering of each TM for CD sample shows fewer changes relative to PR. It is noteworthy that Mn-TM signal increases after 200 cycles for CD. Although a clear explanation is beyond the scope of this study, it is doubtful that Mn might occupy Li/Ni site (2b site), whereas Li ions take position of 4g site, regardless of the larger ionic radius of Li^+ compared to Mn^{4+} for C2/m space group [31]. Future study needs to be made on whether this result represents only for CD sample.

2.4. Role of Na and F in LMR-NMC structure

Based on data from *in situ* XRD and XAS, the activation process diagram of CD during the first cycle is summarized in Fig. 8. Originally, the CD is a nanoscale composition between layered R-3m and C2/m structures, however, the schematic diagram is represented as C2/m since the results show that the dopants have greater effect on the local environment of C2/m phase than R-3m. Partial cation mixing between Ni^{2+} and Li^+ are initially presented, however, with 30% lower for CD akin to PR. Na is believed to play a key part in expanding the Li slab and lessening Ni^{2+}/Li^+ mixing of the pristine structure. When charge between 3.8 V to 4.4 V, mainly Ni^{2+} ions oxidize to Ni^{4+} ions and conventional Li intercalation mechanism undergoes where c-axis expands and a and b-axes contract. A high concentration of Li vacancies in Li layer is generated at this stage. XANES plot shows the evidence that CD utilizes more Ni redox than PR through Ni^{3+} intermediate. At 4.5 V, all Li ions are expected to be extracted from the Li layer with additional capacity from extraction of Li in TM layer coexisting with O 2p redox as shown in the yellow circle along with the TM migration to compensate for charge differences. At this point, F plays an important role in mitigating the oxygen loss, lowering TM migration, and stabilizing lattice $O^{2-}/(O_2)^{n-}$ electron holes as revealed by fitted Mn-O and Ni-O EXAFS spectra. When reaching the highest state of charge, 4.8 V, partial loss of structural ordering is from O_2 loss and irreversible Mn/Ni migration. During discharge to 3.5 V, normal reduction process of TM metals occurs, mainly Ni, and Li ions insert back to Li layer resulting in a and b-axis expansion and c-axis contraction. The local environment of Mn-TM, Ni-O and Co-TM remains unchanged, and CD shows structural irreversibility of only 0.19% after completing the first cycle. Overall, CD enhances structure stability and mitigates voltage fading by tuning the local ordering via Na and F doping, mainly influencing the superstructure C2/m arrangement, and allowing less defect formation upon activation of this material. The more available vacancies from Li/O sites, the more defects there is.

3. Conclusion

Herein, quantitative analysis of structural stability via co-doping Na and F into lattice structure of LMR-NMC during two initial cycles is first reported. From *ex situ* XRD, CD sample shows a 30% lower degree of Li^+/Ni^{2+} mixing in Li layer (4h site) for C2/m structure corresponding to sharper peak of (020) superlattice planes compared to PR sample (before cycle). *In situ* XRD results after activation of Li_2MnO_3-like phase show that the irreversibility of c-axis between first discharge and second charge of PR and CD are contracted by 0.29% and expanded by 0.19%, respectively. After fully charged to 4.8V, the difference of σ^2_{Mn-O} from fitted EXAFS spectra of CD compared to PR is 50% lower providing the ability of CD to minimize the oxygen migration from the structure. From a TM migration perspective, 76% of σ^2_{Ni-TM} is lower in CD than PR attributing to more reversible TM migration. While a certain degree of oxygen is lost in both samples, it is believed that F lowers the need of O redox reaction for charge compensation through the better utilization of Ni redox chemistry (indicated by *in situ* XAS). EXAFS spectra show full recovery of Mn-TM, Co-TM and Ni-O local environment of CD. As a controversy, PR illustrates an increase of cation disordering and the surrounding changes to Ni and Mn after formation cycle.

As a result, Na mainly facilitates the Li diffusion with the expansion of Li layer and enhances cation ordering via substitution in Ni 2b sites while F lessens oxygen loss needed for charge balance during activation cycle, minimizes O 2p redox, utilizes Ni redox capacity, lowers TM migration to Li layer and raises average voltage resulting in a better cycle performance and structure stability. All these are achieved by tuning the local ordering, which in turn decreases defect and vacancy generation from Li/O. Hence, distinct evidence on why CD improves structural stability and reduces voltage degradation is perceived in order to layout a meaningful guidance on the impacts of applying co-dope technique in Li, Mn-rich layered cathode oxides. This may pave the way for the improvement of this high energy cathode materials.

4. Experimental section

4.1. Synthesis of LMR-NMC

The $Mn_{0.54}Ni_{0.13}Co_{0.13}(OH)_2$ precursor was synthesized via hydroxide co-precipitation route followed by solid-state reaction to obtain final cathode powders; $Li_{1.2}Mn_{0.54}Ni_{0.13}Co_{0.13}O_2$ (PR) and $Na_{0.05}Li_{1.15}Mn_{0.54}Ni_{0.13}Co_{0.13}F_{0.01}O_{1.99}$ (CD). Detailed procedures were described elsewhere [27].

4.2. Structural characterization

Crystal structure is studied via high resolution analytical scanning/transmission electron microscopy (S/TEM; FEI Talos F200X) with focused ion beam (Helios 600 Nanolab dualbeam FIB) to provide the cross-section of the particle. Elemental distribution is examined via scanning electron microscopy (SEM; JEOL JSM 7000F) coupled with energy-dispersive X-ray spectroscopy (EDS).

4.3. In situ XRD measurements

High-energy XRD patterns of powder samples and cycling in situ cells were collected at beamline 28-ID-2 XPD of the National Synchrotron Light Source II (NSLS-II) at Brookhaven National Laboratory. The wavelength of the X-ray beam was 0.18208 Å and cesium oxide (CeO_2, NIST SRM 674b) was used as the calibration standard. All XRD patterns were recorded with a Perkin-Elmer XRD 1621 Digital Imaging Detector. The integrated XRD patterns have step size of 0.0038 between 1° to 17°. Rietveld refinements were performed for selected XRD patterns using the FullProf Suite Software. Both $LiMn_{0.5}Ni_{0.5}O_2$ (space group R-3m) and Li_2MnO_3 (space group C2/m) were indexed as the initial structure models.

4.4. In situ XAS measurements

In situ XAS spectra were collected at beamline 7-BM QAS of the National Synchrotron Light Source II (NSLS-II) at Brookhaven National Laboratory via transmission mode. Mn, Co and Ni *K*-edge spectra during 1.5 cycles (0.1C applied to first charge and 0.2C for the rest) were recorded for PR and CD samples. All XAFS data were measured using real-time mode with scanning time of 1 minute for Mn and 30 seconds

for Ni and Co per one spectrum. Reference foils were used for energy calibration and drift correction of the monochromator. The X-ray absorption near edge structure (XANES) spectra were normalized using Athena software [48]. Mn_2O_3, NiO and $LiCoO_2$ were used as reference for data interpretation. The processed extended X-ray absorption fine structure (EXAFS) spectra, $\chi(k)$, was weighted by k^3 to amplify the high-k oscillations. For Fourier-transformed (FT) spectra, the k range between 3.0 to 10.0 $Å^{-1}$ was applied while the fitting in the R range was between 1.0 to 3.0 Å in Artemis software [48] using Li_2MnO_3 (space group C2/m) and $LiNiO_2$ (space group R-3m) as structural references. The paths for fitting are single scattering of O2.1 (first coordination shell), Mn1.1 (second coordination shell), and Ni1.1 (second coordination shell). The fitting k-weight is 2.

4.5. Electrochemical testing

Electrodes were prepared with 80 wt% cathode powder, 10 wt% Super C65 Carbon Black, and 10 wt% of 6 wt% polyvinylidene fluoride (PVDF) dissolved in N-Methyl-2-pyrrolidone (NMP). After completely dried, the electrodes were punched into 10-mm disks. All *in situ* coin cells were assembled in an Argon-filled glove box with an X-ray-transparent window created in the stainless-steel cases and then sealed with Kapton tape (Kapton polyimide film with silicone adhesive) to prevent air exposure. Lithium metal was used as an anode where 1.0 M $LiPF_6$ in EC/EMC (3:7 weight ratio) (Gotion) and 25-μm trilayer polypropylene-polyethylene-polypropylene membrane (MTI) were used as the electrolyte and separator, respectively. GITT and CV were tested using galvanostatic charge/discharge analyzer (Bio-Logic SAS VMP3) with the same coin cell assembly. For GITT, the cells were charged through applying constant current pulse at 0.05C for 30 minutes following by 4-hour relaxation time for each interval. For CV, different scan rate ranging from 0.1 mV s^{-1} to 1.6 mV s^{-1} was collected between 2.50 – 4.80 V (vs. Li/Li^+).

Acknowledgments

The authors appreciatively acknowledge the Department of Chemistry, Chulalongkorn University in collaboration with Bangkok Bank Public Co., Ltd (Thailand) for a graduate fellowship awarded to PV. This research used resources at beamlines 7-BM (QAS) and 28-ID-2 (XPD) of the National Synchrotron Light Source II, and the Center for Functional Nanomaterials under a U.S. Department of Energy (DOE) Office of Science User Facility operated for the DOE Office of Science by Brookhaven National Laboratory (Contract no. DE-SC0012704).

References

[1] M.M. Thackeray, S.-H. Kang, C.S. Johnson, J.T. Vaughey, R. Benedek, S.A. Hackney, Li2MnO3-stabilized LiMO2 (M = Mn, Ni, Co) electrodes for lithium-ion batteries, J. Mater. Chem. 17 (2007) 3112. https://doi.org/10.1039/b702425h.

[2] K. Zhang, B. Li, Y. Zuo, J. Song, H. Shang, F. Ning, D. Xia, Voltage decay in layered Li-rich Mn-based cathode materials, Electrochem. Energy Rev. 2 (2019) 606–623. https://doi.org/10.1007/s41918-019-00049-z.

[3] H. Pan, S. Zhang, J. Chen, M. Gao, Y. Liu, T. Zhu, Y. Jiang, Li- and Mn-rich layered oxide cathode materials for lithium-ion batteries: A review from fundamentals to research progress and applications, Mol. Syst. Des. Eng. 3 (2018) 748–803. https://doi.org/10.1039/c8me00025e.

[4] S. Hu, A.S. Pillai, G. Liang, W.K. Pang, H. Wang, Q. Li, Z. Guo, Li-rich layered oxides and their practical challenges: recent progress and perspectives, electrochem, Energy Rev. 2 (2019) 277–311. https://doi.org/10.1007/s41918-019-00032-8.

[5] W. Yin, A. Grimaud, G. Rousse, A.M. Abakumov, A. Senyshyn, L. Zhang, S. Trabesinger, A. Iadecola, D. Foix, D. Giaume, J.M. Tarascon, Structural evolution at the oxidative and reductive limits in the first electrochemical cycle of Li1.2Ni0.13Mn0.54Co0.13O2, Nat. Commun. (2020) 11. https://doi.org/10.1038/s41467-020-14927-4.

[6] J.R. Croy, M. Balasubramanian, K.G. Gallagher, A.K. Burrell, Review of the U.S. Department of energy's "deep Dive" effort to understand voltage fade in li- and mn-rich cathodes, Acc. Chem. Res. 48 (2015) 2813–2821. https://doi.org/10.1021/acs.accounts.5b00277.

[7] D. Eum, B. Kim, S.J. Kim, H. Park, J. Wu, S.P. Cho, G. Yoon, M.H. Lee, S.K. Jung, W. Yang, W.M. Seong, K. Ku, O. Tamwattana, S.K. Park, I. Hwang, K. Kang, Voltage decay and redox asymmetry mitigation by reversible cation migration in lithium-rich layered oxide electrodes, Nat. Mater. 19 (2020) 419–427. https://doi.org/10.1038/s41563-019-0572-4.

[8] J. Zheng, S. Myeong, W. Cho, P. Yan, J. Xiao, C. Wang, J. Cho, J.G. Zhang, Li- and Mn-rich cathode materials: challenges to commercialization, Adv. Energy Mater. (2017) 7. https://doi.org/10.1002/aenm.201601284.

[9] P.K. Nayak, E.M. Erickson, F. Schipper, T.R. Penki, N. Munichandraiah, P. Adelhelm, H. Sclar, F. Amalraj, B. Markovsky, D. Aurbach, Review on challenges and recent advances in the electrochemical performance of high capacity li- and Mn-rich cathode materials for li-ion batteries, Adv. Energy Mater. 8 (2018) 1–16. https://doi.org/10.1002/aenm.201702397.

[10] G. Chen, J. An, Y. Meng, C. Yuan, B. Matthews, F. Dou, L. Shi, Y. Zhou, P. Song, G. Wu, D. Zhang, Cation and anion Co-doping synergy to improve structural stability of Li- and Mn-rich layered cathode materials for lithium-ion batteries, Nano Energy 57 (2019) 157–165. https://doi.org/10.1016/j.nanoen.2018.12.049.

[11] D. Liu, X. Fan, Z. Li, T. Liu, M. Sun, C. Qian, M. Ling, Y. Liu, C. Liang, A cation/anion co-doped Li 1.12 Na 0.08 Ni 0.2 Mn 0.6 O 1.95 F 0.05 cathode for lithium ion batteries, Nano Energy 58 (2019) 786–796. https://doi.org/10.1016/j.nanoen.2019.01.080.

[12] L. Ming, B. Zhang, Y. Cao, J.-F. Zhang, C.-H. Wang, X.-W. Wang, H. Li, Effect of Nb and F Co-doping on Li1.2Mn0.54Ni0.13Co0.13O2 cathode material for high-performance lithium-ion batteries, Front. Chem 6 (2018) 1–12. https://doi.org/10.3389/fchem.2018.00076.

[13] S.N. Lim, J.Y. Seo, D.S. Jung, S. Bin Park, S.H. Yeon, The crystal structure and electrochemical performance of Li1.167Mn0.548Ni0.18Co0.105O2 composite cathodes doped and co-doped with Mg and F, J. Electroanal. Chem. 740 (2015) 88–94. https://doi.org/10.1016/j.jelechem.2015.01.010.

[14] K. Du, F. Yang, G.R. Hu, Z.D. Peng, Y.B. Cao, K.S. Ryu, Sodium additive to improve rate performance of Li[Li0.2Mn 0.54Ni0.13Co0.13]O2 material for Li-ion batteries, J. Power Sources 244 (2013) 29–34. https://doi.org/10.1016/j.jpowsour.2013.04.152.

[15] R.P. Qing, J.L. Shi, D.D. Xiao, X.D. Zhang, Y.X. Yin, Y.B. Zhai, L. Gu, Y.G. Guo, Enhancing the kinetics of Li-rich cathode materials through the pinning effects of gradient surface Na + Doping, Adv. Energy Mater. 6 (2016) 1–6. https://doi.org/10.1002/aenm.201501914.

[16] S. Chen, Z. Chen, M. Xia, C. Cao, Y. Luo, Toward alleviating voltage decay by sodium substitution in lithium-rich manganese-based oxide cathodes, ACS Appl. Energy Mater. 1 (2018) 4065–4074. https://doi.org/10.1021/acsaem.8b00740.

[17] Y. Liu, D. Liu, H.H. Wu, X. Fan, A. Dou, Q. Zhang, M. Su, Improved cycling stability of Na-doped cathode materials Li1.2Ni0.2Mn0.6O2 via a Facile Synthesis, ACS Sustain. Chem. Eng. 6 (2018) 13045–13055. https://doi.org/10.1021/acssuschemeng.8b02552.

[18] W. He, P. Liu, B. Qu, Z. Zheng, H. Zheng, P. Deng, P. Li, S. Li, H. Huang, L. Wang, Q. Xie, D.L. Peng, Uniform Na + Doping-induced defects in Li- and Mn-rich cathodes for high-performance lithium-ion batteries, Adv. Sci. (2019) 1802114. https://doi.org/10.1002/advs.201802114.

[19] L. Li, B.H. Song, Y.L. Chang, H. Xia, J.R. Yang, K.S. Lee, L. Lu, Retarded phase transition by fluorine doping in Li-rich layered Li 1.2 Mn 0.54 Ni 0.13 Co 0.13 O 2 cathode material, J. Power Sources 283 (2015) 162–170. https://doi.org/10.1016/j.jpowsour.2015.02.085.

[20] S.H. Lee, J.S. Moon, M.S. Lee, T.H. Yu, H. Kim, B.M. Park, Enhancing phase stability and kinetics of lithium-rich layered oxide for an ultra-high performing cathode in Li-ion batteries, J. Power Sourc. 281 (2015) 77–84. https://doi.org/10.1016/j.jpowsour.2015.01.158.

[21] J.H. Song, A. Kapylou, H.S. Choi, B.Y. Yu, E. Matulevich, S.H. Kang, Suppression of irreversible capacity loss in Li-rich layered oxide by fluorine doping, J. Power Sourc. 313 (2016) 65–72. https://doi.org/10.1016/j.jpowsour.2016.02.058.

[22] S. Krishna Kumar, S. Ghosh, P. Ghosal, S.K. Martha, Synergistic effect of 3D electrode architecture and fluorine doping of Li 1.2 Ni 0.15 Mn 0.55 Co 0.1 O 2 for

high energy density lithium-ion batteries, J. Power Sourc. 356 (2017) 115–123. https://doi.org/10.1016/j.jpowsour.2017.04.077.
[23] Y. Wang, H.T. Gu, J.H. Song, Z.H. Feng, X. Bin Zhou, Y.N. Zhou, K. Wang, J.Y. Xie, Suppressing Mn reduction of Li-rich Mn-based cathodes by F-Doping for advanced lithium-ion batteries, J. Phys. Chem. C. 122 (2018) 27836–27842. https://doi.org/10.1021/acs.jpcc.8b08669.
[24] W.D. Richards, S.T. Dacek, D.A. Kitchaev, G. Ceder, Fluorination of lithium-excess transition metal oxide cathode materials, Adv. Energy Mater. 8 (2018) 1–7. https://doi.org/10.1002/aenm.201701533.
[25] R.J. Clément, D. Kitchaev, J. Lee, Gerbrand Ceder, Short-range order and unusual modes of nickel redox in a fluorine-substituted disordered rocksalt oxide lithium-ion cathode, Chem. Mater. 30 (2018) 6945–6956. https://doi.org/10.1021/acs.chemmater.8b03794.
[26] J. Lee, J.K. Papp, R.J. Clément, S. Sallis, D.H. Kwon, T. Shi, W. Yang, B.D. McCloskey, G. Ceder, Mitigating oxygen loss to improve the cycling performance of high capacity cation-disordered cathode materials, Nat. Commun. (2017) 8. https://doi.org/10.1038/s41467-017-01115-0.
[27] P. Vanaphuti, J. Chen, J. Cao, K. Bigham, B. Chen, L. Yang, H. Chen, Y. Wang, Enhanced electrochemical performance of the lithium-manganese-rich cathode for li-ion batteries with Na and F CoDoping, ACS Appl. Mater. Interfaces 11 (2019) 37842–37849. https://doi.org/10.1021/acsami.9b13838.
[28] E. Deiss, Spurious chemical diffusion coefficients of Li+ in electrode materials evaluated with GITT, Electrochim. Acta 50 (2005) 2927–2932. https://doi.org/10.1016/j.electacta.2004.11.042.
[29] F. Wu, G. Kim, M. Kuenzel, H. Zhang, J. Asenbauer, D. Geiger, U. Kaiser, S. Passerini, Elucidating the effect of iron doping on the electrochemical performance of cobalt-free lithium-rich layered cathode materials, Adv. Energy Mater. (2019) 1902445. https://doi.org/10.1002/aenm.201902445.
[30] P. Vanaphuti, S. Bong, L. Ma, S. Ehrlich, Y. Wang, Systematic study of different anion doping on the electrochemical performance of cobalt-free lithium–manganese-rich layered cathode, ACS Appl. Energy Mater. 3 (2020) 4852–4859. https://doi.org/10.1021/acsaem.0c00439.
[31] D. Mohanty, A. Huq, E.A. Payzant, A.S. Sefat, J. Li, D.P. Abraham, D.L. Wood, C. Daniel, Neutron diffraction and magnetic susceptibility studies on a high-voltage Li1.2Mn0.55Ni0.15Co0.10O 2 lithium ion battery cathode: Insight into the crystal structure, Chem. Mater. 25 (2013) 4064–4070. https://doi.org/10.1021/cm402278q.
[32] W. Xiang, C.Q. Zhu, J. Zhang, H. Shi, Y.T. Liang, M.H. Yu, X.M. Zhu, F.R. He, G.P. Lv, X.D. Guo, Synergistic coupling effect of sodium and fluorine co-substitution on enhancing rate capability and cycling performance of Ni-rich cathode for lithium ion battery, J. Alloys Compd. 786 (2019) 56–64. https://doi.org/10.1016/j.jallcom.2019.01.264.
[33] J.R. Lu, Z. Dahn, Understanding the Anomalous Capacity of Li / Li [Ni x Li (1 / 3 − 2x / 3) Mn (2 / 3 − x / 3)] O 2 cells using in situ x-ray diffraction and electrochemical studies, J. Electrochem. Soc. 149 (2002) A815. https://doi.org/10.1149/1.1480014.
[34] S. Hy, H. Liu, M. Zhang, D. Qian, B.J. Hwang, Y.S. Meng, Performance and design considerations for lithium excess layered oxide positive electrode materials for lithium ion batteries, Energy Environ. Sci. 9 (2016) 1931–1954. https://doi.org/10.1039/c5ee03573b.
[35] J.R. Croy, A. Gutierrez, M. He, B.T. Yonemoto, E. Lee, M.M. Thackeray, Development of manganese-rich cathodes as alternatives to nickel-rich chemistries, J. Power Sourc. 434 (2019) 226706. https://doi.org/10.1016/j.jpowsour.2019.226706.
[36] M. Sathiya, G. Rousse, K. Ramesha, C.P. Laisa, H. Vezin, M.T. Sougrati, M.L. Doublet, D. Foix, D. Gonbeau, W. Walker, A.S. Prakash, M. Ben Hassine, L. Dupont, J.M. Tarascon, Reversible anionic redox chemistry in high-capacity layered-oxide electrodes, Nat. Mater 12 (2013) 827–835. https://doi.org/10.1038/nmat3699.
[37] F. Dogan, B.R. Long, J.R. Croy, K.G. Gallagher, H. Iddir, J.T. Russell, M. Balasubramanian, B. Key, Re-entrant lithium local environments and defect driven electrochemistry of Li- and Mn-rich Li-Ion battery cathodes, J. Am. Chem. Soc. 137 (2015) 2328–2335. https://doi.org/10.1021/ja511299y.
[38] A. Ito, Y. Sato, T. Sanada, M. Hatano, H. Horie, Y. Ohsawa, In situ X-ray absorption spectroscopic study of Li-rich layered cathode material Li[Ni0.17Li0.2Co0.07Mn 0.56]O2, J. Power Sourc. 196 (2011) 6828–6834. https://doi.org/10.1016/j.jpowsour.2010.09.105.
[39] H. Koga, L. Croguennec, M. Ménétrier, P. Mannessiez, F. Weill, C. Delmas, S. Belin, Operando x-ray absorption study of the redox processes involved upon cycling of the li-rich layered oxide Li1.20Mn0.54Co 0.13Ni0.13O2 in li ion batteries, J. Phys. Chem. C. 118 (2014) 5700–5709. https://doi.org/10.1021/jp412197z.
[40] G. Assat, A. Iadecola, D. Foix, R. Dedryvere, J.M. Tarascon, Direct quantification of anionic redox over long cycling of li-rich nmc via hard x-ray photoemission spectroscopy, ACS Energy Lett. 3 (2018) 2721–2728. https://doi.org/10.1021/acsenergylett.8b01798.
[41] J.R. Croy, K.G. Gallagher, M. Balasubramanian, B.R. Long, M.M. Thackeraya, Quantifying hysteresis and voltage fade in xLi2MnO 3 (1-x)LiMn0.5Ni0.5O2 electrodes as a function of Li2MnO3 content, J. Electrochem. Soc. 161 (2014) 318–325. https://doi.org/10.1149/2.049403jes.
[42] E. Hu, X. Yu, R. Lin, X. Bi, J. Lu, S. Bak, K.W. Nam, H.L. Xin, C. Jaye, D.A. Fischer, K. Amine, X.Q. Yang, Evolution of redox couples in Li- and Mn-rich cathode materials and mitigation of voltage fade by reducing oxygen release, Nat. Energy 3 (2018) 690–698. https://doi.org/10.1038/s41560-018-0207-z.
[43] K. Luo, M.R. Roberts, R. Hao, N. Guerrini, D.M. Pickup, Y.S. Liu, K. Edström, J. Guo, A.V. Chadwick, L.C. Duda, P.G. Bruce, Charge-compensation in 3d-transition-metal-oxide intercalation cathodes through the generation of localized electron holes on oxygen, Nat. Chem. 8 (2016) 684–691. https://doi.org/10.1038/nchem.2471.
[44] M. Li, T. Liu, X. Bi, Z. Chen, K. Amine, C. Zhong, J. Lu, Cationic and anionic redox in lithium-ion based batteries, Chem. Soc. Rev. (2020). https://doi.org/10.1039/c8cs00426a.
[45] G. Assat, J.M. Tarascon, Fundamental understanding and practical challenges of anionic redox activity in Li-ion batteries, Nat. Energy 3 (2018) 373–386. https://doi.org/10.1038/s41560-018-0097-0.
[46] R.A. House, U. Maitra, M.A. Pérez-osorio, J.G. Lozano, L. Jin, J.W. Somerville, L.C. Duda, A. Nag, A. Walters, K. Zhou, M.R. Roberts, P.G. Bruce, Superstructure control of first-cycle voltage hysteresis in O-redox cathodes, Nature 577 (2020) 502–508. https://doi.org/10.1038/s41586-019-1854-3.
[47] Y. Yu, P. Karayaylali, S.H. Nowak, L. Giordano, M. Gauthier, W. Hong, R. Kou, Q. Li, J. Vinson, T. Kroll, D. Sokaras, C.-J. Sun, N. Charles, F. Maglia, R. Jung, Y. Shao-Horn, Revealing electronic signatures of lattice oxygen redox in lithium ruthenates and implications for high-energy li-ion battery material designs, Chem. Mater. 31 (2019) 7864–7876. https://doi.org/10.1021/acs.chemmater.9b01821.
[48] B. Ravel, M. Newville, ATHENA, ARTEMIS, HEPHAESTUS: data analysis for X-ray absorption spectroscopy using IFEFFIT, J. Synchrotron Radiat. 12 (2005) 537–541. https://doi.org/10.1107/S0909049505012719.